



---

Final Report for MEng Project

---

**Development of MRI T2\* Mapping  
Model for N-Periodic ka-SPGR Sequence:  
A Promising Technique for Parkinson's  
Disease Biomarker Detection**

---

Author name: Yifei Jin  
Supervisor: Dr. Neal K. Bangerter

Submitted in partial fulfilment of the requirements for the award of  
MEng in Biomedical Engineering from Imperial College London

Thursday, 15 June 2023 Word count: 4361

## Contents

<b>1 Abstract</b>	<b>3</b>
<b>2 Introduction</b>	<b>4</b>
<b>3 Theory</b>	<b>6</b>
3.1 Multi-echo SPGR . . . . .	6
3.2 N-periodic ka-SPGR . . . . .	7
<b>4 Methods</b>	<b>8</b>
4.1 Model Simulation and Analysis . . . . .	8
4.1.1 Simulation setup . . . . .	8
4.1.2 Data simulation . . . . .	9
4.1.3 Analysis method . . . . .	10
4.2 MRI Data Acquisition and Analysis . . . . .	10
4.2.1 MRI scan setup . . . . .	10
4.2.2 Image processing . . . . .	11
4.2.3 Analysis method . . . . .	12
<b>5 Results</b>	<b>13</b>
5.1 Model simulation results . . . . .	13
5.1.1 Optimal N-periodic ka-SPGR parameter . . . . .	13
5.1.2 Optimal N-periodic ka-SPGR accuracy and precision . . . . .	14
5.2 Phantom MRI scan results . . . . .	14
5.2.1 Quantitative T2* mapping image . . . . .	14
5.2.2 Percentage bias . . . . .	15
5.2.3 Effective T2* Signal-to-Noise (SNR) ratio . . . . .	16
<b>6 Discussion and Conclusion</b>	<b>17</b>
<b>7 Acknowledgements</b>	<b>19</b>
<b>References</b>	<b>20</b>

## 1 Abstract

Early diagnosis and tracking of Parkinson's disease (PD) can be achieved by detecting the excessive iron at substantia nigra (SN) with MRI relaxometry parameter T2\*, unfortunately, accurate high-resolution T2\* mapping imaging is difficult to perform at the brain stem due to tissue motion. A novel technique N-periodic ka-SPGR is proposed to be motion robust and can be used to acquire quantitative T2\* mapping images, while neither analysis of the techniques' T2\* mapping performance nor optimised scan parameters were suggested. This study provides optimised parameters (period and repetition time) of ka-SPGR specifically for PD biomarker detection based on a computer simulation. It is followed by a phantom scanning experiment with the optimised ka-SPGR sequence, and the T2\* mapping result of the multi-echo SPGR sequence is used as the gold standard to compare with. 7-periodic or 12-periodic ka-SPGR with a repetition time of 6ms is suggested to optimise the performance. The 12-periodic ka-SPGR is more robust to noise, while the 7-periodic provides better efficiency. The accuracy and precision of both sequences are proven by the simulation and phantom experiment results, which both show a percentage bias  $< \pm 10\%$ . However, the study is limited by the phantom's misalignment with the SN and can be improved using a phantom specifically adjust for SN tissue property. Additionally, to further prove the reliability of N-periodic ka-SPGR for PD biomarker detection, massive in-vivo experiments are desirable to evaluate its performance in realistic and complex environments.

## 2 Introduction

Parkinson's disease (PD) is a chronic neurodegenerative disease that affects the motor region of the brain and causes tremors, it is the second most common neurodegenerative disorder and approximately 9.4 million people suffer from PD worldwide [19, 16]. The disease's pathophysiology is irreversible and currently has no cure. Therefore, early detection and accurate progress tracking are essential for supporting PD treatment and new solution development, which can be achieved by having effective biomarkers. One of the PD's early signs is iron deposition in the substantia nigra (SN) region in the brain stem, as shown in Figure 1 [6, 15, 3], which can be detected using Magnetic Resonance Imaging (MRI) techniques [2, 13].

MRI is a non-invasive medical imaging technique. It constructs images based on the proton's signal responses to a train of radiofrequency excitations and pulsed magnetic field gradients (pulse sequence) under different chemical environments. The MRI signal decays exponentially with the tissue and field inhomogeneity-dependent time constant  $T2^*$  and the amount of  $T2^*$  decay of the signal acquired is determined by the choice of echo time (TE), the relationship can be described by the equation  $S(TE) \propto e^{-\frac{TE}{T2^*}}$ . As the excessive iron caused by PD distorts the magnetic field, a more rapid decay of the MRI signal and a smaller  $T2^*$  value will be observed at the SN, various studies have shown this change of  $T2^*$  value can be used as an effective biomarker for PD [3, 15]. A traditional way of generating quantitative  $T2^*$  images is to acquire MR images at different TEs and fit the signal's exponential decay in each voxel to get the  $T2^*$ , this technique is known as  $T2^*$  mapping using a Multi-Echo Spoiled Gradient-Recalled (multi-echo SPGR) sequence [5]. However, the complex tissue movement at the brain stem, which is related to blood flow, central cerebellum fluid flow, and the cardiac cycle, results in tissue motion artefacts on MR images and makes high-quality brain stem MRI difficult to achieve [20, 11]. Additionally, it makes getting an accurate  $T2^*$  mapping image of the brain even more difficult as one such image is constructed based on multiple high-quality MR images.

A simple way to reduce the effect of tissue motion is acquiring multiple MR images and averaging to reduce motion artefacts, but it will lengthen the acquisition time. Using a larger voxel size can also reduce the impact of the tissue movement, however, high-resolution MR images are essential to capture important tissue information from the tiny millimetre-size nigrosomes, which are iron-rich subregions of the SN where PD-related changes first build up [20]. Other post-processing-based methods can perform motion correction on the acquired images, but these techniques mostly focus on the rigid whole-body movement instead of the complex non-rigid tissue motion [14].

Based on all these limitations, a new  $T2^*$  imaging technique is suggested [12], which can reduce the impact of motion while maintaining short acquisition time and good resolution, using the MRI pulse sequence named k-space-aliased Spoiled Gradient-Recalled (ka-SPGR). The images acquired with ka-SPGR are not simply related by decay time, instead, each image is a complex summation of signal from multiple TEs. By extracting each signal component of this complex sum, the  $T2^*$  related signal decay at specific TEs can be reconstructed and  $T2^*$  can be calculated by fitting the exponential decay. Theoretically, even if the movement of the brain creates

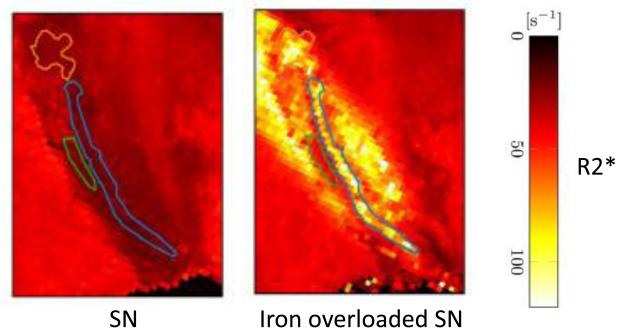


Figure 1: The iron overload in the substantia nigra can be detected using the MRI technique  $R2^*$  mapping, where  $R2^*$  equals  $\frac{1}{T2^*}$ . (Brammerloh, Malte et al., 2021)

artefacts in some acquisition, it will not have a huge impact on the reconstructed T2\* decay signal, as the signal is obtained by averaging across multiple acquisitions. However, so far there has not yet been any quantitative analysis of the ka-SPGR T2\* measurement accuracy compared to the standard multi-echo SPGR approach, and no suggested optimal MRI scanning parameters for the ka-SPGR sequence. Therefore, evaluating the ka-SPGR's T2\* accuracy and obtaining optimal parameters is desirable, before examining the motion robustness of the ka-SPGR technique *in vivo*.

The aim and objectives of this project are the following:

1. Model the ka-SPGR T2\* measurement based on Bloch simulation, followed by Monte Carlo tests to analyse the bias and variation of the measured T2\* when acquisition noise is considered.
2. Suggest optimal scan parameters based on analysis of the simulation results.
3. Acquire MRI data from a phantom using the gold-standard technique (multi-echo SPGR) and ka-SPGR with optimised parameters.
4. Compare the reconstructed quantitative T2\* mapping images of the gold-standard technique and ka-SPGR.
5. Compute the T2\* percentage error and T2\* effective signal-to-noise ratio of the acquired data to evaluate the practical performance of ka-SPGR and compare it with the gold-standard technique.

### 3 Theory

In MRI, a train of radiofrequency (RF) pulse sequences excites the magnetised spins to generate the MRI signal. During excitation, the magnetisation initially aligned with the main magnetic field in the longitudinal direction is tipped towards the transverse plane with a longitudinal flip of  $\alpha^\circ$  and a transverse phase shift  $\phi$ . After the excitation, the magnetisation relaxes with a longitudinal regrowth with the time constant T1 and a transverse decay. The transverse component of magnetisation is measured to form an MR image and the signal will decay with a time constant T2 or T2\* depending on the MRI pulse sequence used. The time between excitation and acquisition of the signal is known as echo time (TE), and the time between adjacent excitations is repetition time (TR). The MRI signal is acquired in Fourier space, known as k-space, and the resulting image is reconstructed by performing the inverse Fourier transform of the acquired k-space. The two types of MRI pulse sequences used in this project are briefly introduced below. [18]

#### 3.1 Multi-echo SPGR

Using a spoiled gradient-recalled (SPGR) based pulse sequence, the acquired MR signal decays with the time constant T2\* [4]. The gold-standard T2\* measuring technique – multi-echo SPGR is performed by measuring the MR signal at multiple TEs in one TR with a SPGR sequence and fitting monoexponential decay to get the time constant T2\* voxel by voxel as shown in Figure 2a

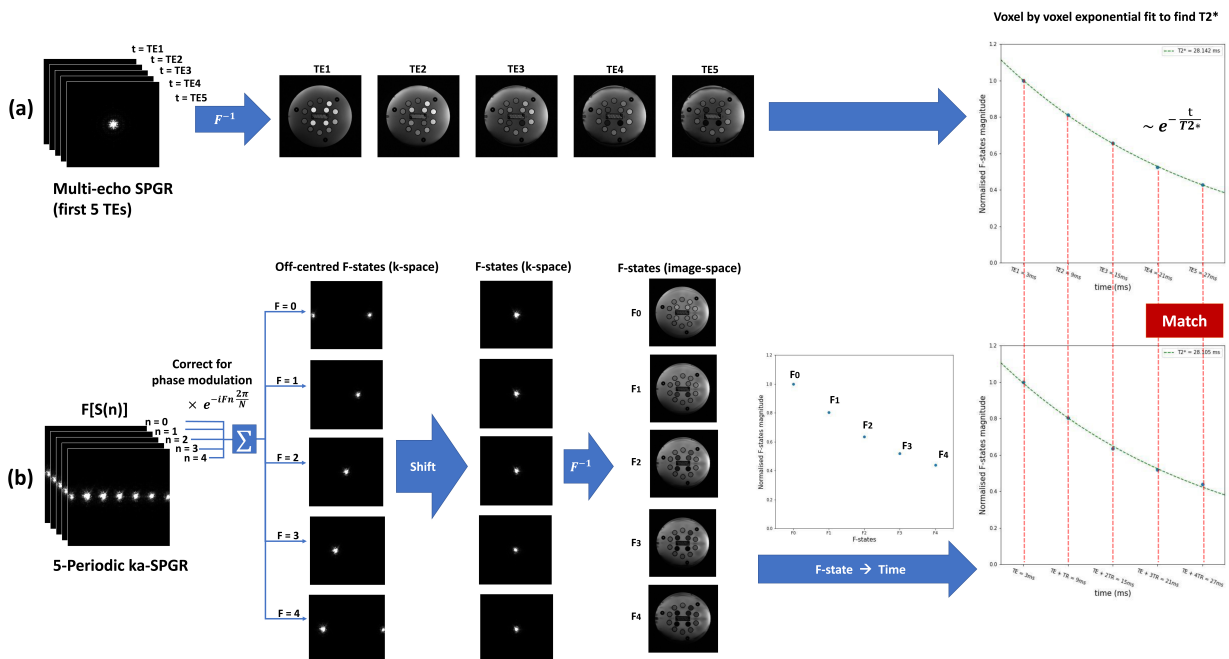


Figure 2: Flow charts of multi-echo SPGR (a) and N-periodic ka-SPGR (b) image formation and T2\* calculation process.

Starting from the raw k-space data acquired by the MRI scanner (left) to the voxel-by-voxel exponential fit for T2\* value calculation (right). K-spaces and images of 5-echo SPGR and 5-periodic ka-SPGR are used to aid illustration. The matching of the two techniques for comparison purposes, which will be discussed in the Method section, is shown in the exponential fitting figures on the right.

### 3.2 N-periodic ka-SPGR

The N-periodic ka-SPGR sequence is based on short TR fast SPGR [7] with  $TE = TR/2$ . The repeated excitation with short TR leads to the formation of a steady-state signal. Additionally, radiofrequency-spoiling (RF-spoiling) is applied by incrementing the RF excitation phase with a quadratic series, as shown in the equation below [7, 12],

$$\phi_n = 0.5 \times n^2 \times \frac{2\pi}{N}, (n = 0, 1, 2\dots), \quad (1)$$

where  $n$  is the index of the RF excitation, and  $N$  is the chosen periodicity. By using this quadratically changing excitation phase, the signal acquired after the RF excitation will periodically yield  $N$  different steady-states  $S(0), S(1) \dots S(N - 1)$ . The analytical solution of the steady-state signal after the  $n^{th}$  RF pulse is shown below[12],

$$S(n) = e^{i\omega TE} \sum_F A e^{-(TE+F \times TR)/T2^*} e^{iF\omega TR} e^{inF \frac{2\pi}{N}}, F \in \mathbb{Z} : F \geq 0 \quad (2)$$

where  $\omega$  is the off-resonance frequency,  $A$  is a constant,  $F$  is the F-state index, and the  $e^{i\omega TE}$  and  $e^{iF\omega TR}$  terms relate to the off-resonance precession. Each steady-state signal is the summation of the  $T2^*$  dependent signals at specific times ( $Ae^{-(TE+F \times TR)/T2^*}$ ) weighted by corresponding phase modulation ( $e^{inF \frac{2\pi}{N}}$ ). This  $T2^*$  dependent component in the equation,  $Ae^{-(TE+F \times TR)/T2^*}$ , is known as the configuration state or F-state signal and is denoted as  $F_0$  if  $F$  in the equation equals 0. For a given acquisition, the user can choose how many F-state components are included in the measured signal by adjusting a spoiler gradient in the sequence. This shifts the different F-state signals apart from each other in k-space, as shown in Figure 3. Notice that the ideal case will be having exactly  $N$  F-states in the acquired signal.

The k-space of each F-state can be reconstructed by summing up  $N$ -acquired signals after negating the corresponding phase modulation with  $e^{-inF \frac{2\pi}{N}}$ , followed by shifting the k-space back to the centre. An inverse Fourier transform is then performed to generate the F-states images. The F-states magnitudes are then used to perform a monoexponential decay fit with scaled effective echo times ( $TE + F \times TR$ ) for acquiring  $T2^*$ . An illustration of this procedure using 5-periodic ka-SPGR is provided in Figure 2b.

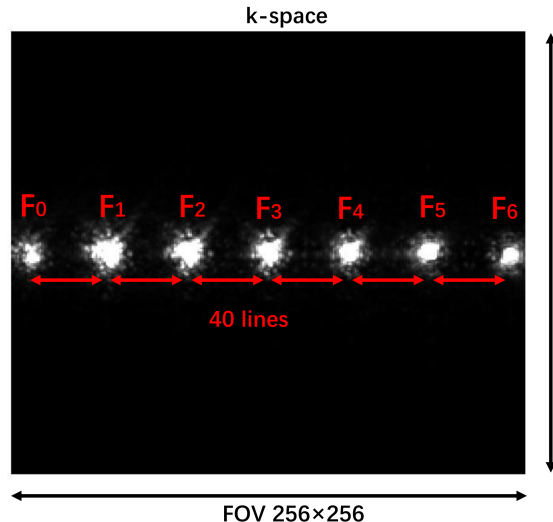


Figure 3: The F-states are shifted apart in the k-space by a 40 lines shift spoiler gradient for an image with  $256 \times 256$  FOV.

$F_0 - F_6$  components are included in this measured signal.

## 4 Methods

### 4.1 Model Simulation and Analysis

A Python-based computer simulation was built to model the ka-SPGR T2\* mapping performance when using different TR and N. The simulated results were then used to find the optimal ka-SPGR parameters for PD biomarker detection. The full version of the Python code for simulation, image reconstruction and analysis is provided in the following GitHub repository: [https://github.com/Yifei-Jin/Final\\_Year\\_Project.git](https://github.com/Yifei-Jin/Final_Year_Project.git)

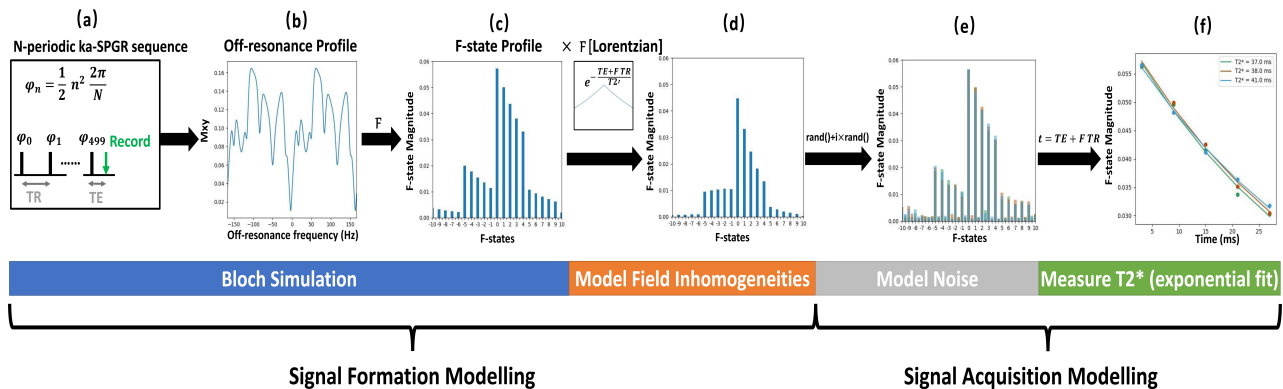


Figure 4: N-periodic ka-SPGR computer simulation flow chart (a) The N-periodic ka-SPGR sequence configuration (b) Off-resonance profile of 6ms TR 5-periodic ka-SPGR (c) F-state profile and the Lorentzian for modelling field inhomogeneities (d) F-state profile with field inhomogeneities corresponding to  $T2^* = 40\text{ms}$  (e) F-state profile of 3 random acquisitions plotted using different coloured bars. (f)  $T2^*$  fitting using the 3 random acquisition data

#### 4.1.1 Simulation setup

As shown in Figure 4, the computer simulation can be described in 2 sections - signal formation modelling, where the ideal Bloch simulation is performed followed by applying the magnetic field inhomogeneities; and acquisition modelling, where the noise is considered and  $T2^*$  fitting is performed.

- Bloch Simulation

Using the well known Bloch equation [18], the performance of the spin with specific tissue properties ( $T1$ ,  $T2$ ) under different applied pulse sequences was modelled by applying specific  $\alpha$ ,  $\phi$ , TR and TE. As the

Simulation Parameters	T2	44 ms
	T1	800 ms
	Number of different off-resonance frequencies	1000
	Flip angle, $\alpha$	10
	Initial magnetisation, $M0$	1
	Number of TR before record signal	500
	Sample size	1000
	N	3~12
Data Simulation Range	TR range	2~10ms (0.4 ms increment)
	$T2^*$ range	13~53 ms (1 ms increment)

Table 1: Computer simulation parameters and range

project focused on SN region T2\* mapping, SN's T1 (800ms) and T2 (44ms) were used in the computer simulation model, suggested by previous research on SN [17, 3]. A 10° optimal flip angle calculated from the Ernst equation was used [8], and RF-spoiling was applied by implementing phase shift  $\phi$  based on equation (1). Additionally, to ensure the steady state is fully reached, the spin was repeatedly excited 500 times before acquiring the signal. The structure of the pulse sequence is shown in the left first figure in Figure 4, and the parameters used are summarised in Table 1. An off-resonance profile was then generated, as shown in Figure 4b, which models the performance of spins under external disturbances by simulating spins with different extra phase shifts, and the Fourier transform of the off-resonance profile is equal to the configuration F-states, as shown in Figure 4c [22].

- Magnetic field inhomogeneities modelling

The field inhomogeneities effect caused by excessive iron in the tissue can be modelled by convolving the Lorentzian distributed field inhomogeneities with the off-resonance profile [23]. With a selected ground truth T2\* and the known SN T2, the inhomogeneities effect related to the ground truth T2\* can be calculated using the relationship [4],

$$\frac{1}{T2^*} = \frac{1}{T_2} + \gamma \Delta B_{inhomogeneities} \quad (3)$$

and applied to the Bloch simulation model. However, as shown in Figure 4d, in this computer simulation, multiplying the F-states signal with the Fourier transform of Lorentzian - an exponential curve with the time constant  $T2' = \frac{1}{\gamma \Delta B_{inhomogeneities}}$  was performed instead of the complicated convolution, as it is an equivalent operation supported by the property of Fourier transforms.

- Noise modelling

In reality, an MRI scanner introduces noise while acquiring the signal [10]. For ka-SPGR with different N and TR, the acquisition noise was modelled using zero-mean Gaussian with standard deviation equals  $\frac{F_0}{\sqrt{N}} \times 5\%$ , where the  $F_0$  is the  $F_0$ -state magnitude simulated when  $T2^* = 33\text{ms}$ , the mean of PD and healthy SN T2\*. Then the generated Gaussian noise was added to the imaginary and real parts of the simulated F-states signal. Figure 4e shows 3 times of F-state acquisition modelling, each different colour indicates one sample acquisition. Additionally, in the data simulation, 1000 acquisitions were made to perform the Monte Carlo experiment and analyse the performance.

- T2\* measurement modelling

To model the T2\* calculation of N-periodic ka-SPGR, the exponential fit should only use the first N F-state magnitude  $F_0 \dots F_{N-1}$ , because only these F-states can be reconstructed from the acquired signal using N-periodic ka-SPGR.(i.e. we can only recover N signal components from N separate acquisitions) As shown in Figure 4f, only the first 5 F-states were used to fit the exponential for 5-periodic ka-SPGR.

#### 4.1.2 Data simulation

The data were simulated for spins with ground truth T2\* of 13-53ms when applying 3 - 12 periodic ka-SPGR sequences with different TRs from 2ms to 10ms. The bottom section of Table 1 summarised the scan parameters covered by the data simulation. The range of ground truth T2\* was selected specifically for analysing PD biomarker detection accuracy, which is between the PD patients' (13ms) and healthy SN T2\* (53ms) [3]. The above N and TR ranges were selected for the simulation because an N less than 3 is not able to provide enough data points for fitting the exponential curve, and a TR smaller than 2ms cannot be achieved by a clinical scanner, also, N greater than 12 or TR greater than 10ms both leads to an unacceptable long acquisition time.

On top of the selected range, Monte Carlo experiments were performed and by fitting each group of acquired

F-states, 1000 measured  $T2^*$  can be obtained for each ground truth  $T2^*$  value for different periodic ka-SPGR with different TR.

#### 4.1.3 Analysis method

The simulated  $T2^*$  were then further analysed using percentage bias and standard deviation to find optimal scan parameters. The percentage bias of the simulated  $T2^*$  shows the accuracy of the  $T2^*$  measurement and it largely depends on the choice of N and TR. As shown in Figure 4, the effective echo time of points used for exponential fit is  $TE + F \times TR, F = 0 \dots (N - 1)$ , by using different N and TR, different regions and ranges of the exponential curve are sampled, which will affect the accuracy of the exponential fit. By locating the minimum average percentage bias, the optimal N and TR for ka-SPGR that maximises  $T2^*$  measurement accuracy were found. The standard deviation of the measured  $T2^*$  using the optimised parameter was then computed to evaluate the variation of the measurement and verify the reliability of the technique. According to [3] the iron-induced change in SN  $T2^*$  is  $40ms \pm 6.5ms$ , which has a 16% percentage error, to detect the change, a  $T2^*$  percentage error  $< 5\%$  would be acceptable. Once the accuracy and precision of the chosen parameter were proven, it was then used for the MRI phantom scanning experiment.

## 4.2 MRI Data Acquisition and Analysis

An MRI scan using the ka-SPGR sequence with optimised scan parameters was performed on a phantom. The  $T2^*$  values were calculated and compared with the ground truth  $T2^*$  value obtained using the gold-standard multi-echo SPGR technique. Followed by a comparison between the ka-SPGR and the multi-echo SPGR techniques with matched acquisition conditions.

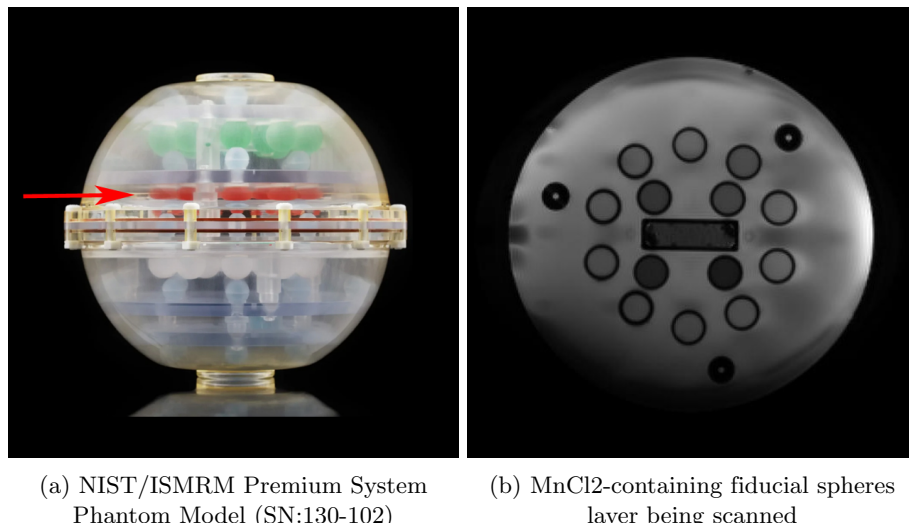


Figure 5: The phantom used for the scanning experiment.  
The red arrow in (a) shows the  $MnCl_2$ -containing layer where the scan is performed

#### 4.2.1 MRI scan setup

NIST/ISMRM Premium System Phantom Model (SN:130-102) shown in Figure 5a was used as the scanning object, and a slice acquisition was performed at the  $MnCl_2$ -containing fiducial spheres layer (Figure 5b), which contains multiple spheres with varying  $T2^*$  over a wide range. Multi-echo FLASH (Siemens, 3T), one commonly used multi-echo SPGR sequence, was used as the gold standard  $T2^*$  measuring technique to obtain the ground truth  $T2^*$  value for each fiducial sphere.

MRI signals were acquired from the phantom using 7 and 12-periodic ka-SPGR sequences with TR = 6ms and 10° flip angle, which were optimised using the computer simulation. The range of F-states and amount of gradient spoiler shift were carefully selected (Table 2b) to make sure the required N F-states are separated while still within the k-space acquisition range.

MRI signals were also acquired using multi-echo SPGR with parameters chosen to match with ka-SPGR. In order to minimise the influence of the exponential fitting efficiency, the number and position of data points used to fit the exponential curve were kept consistent for the two techniques. Therefore, to achieve the match shown in Figure 2, the multi-echo SPGR TEs started with ka-SPGR's TE and following by an increment equal to ka-SPGR's TR as shown in Table 2a. Additionally, the number was kept consistent by using the first N acquisition of multi-echo SPGR to fit exponential fit when compare with N-periodic ka-SPGR. Also, the image and voxel sizes were matched for all scanning performed, as shown in Table 2.

A 90° flip angle multi-echo SPGR was used to obtain an accurate T2\* ground truth value for evaluating ka-SPGR T2\* accuracy, and a 20° flip angle multi-echo SPGR was used to match with ka-SPGR's flip angle aiming at comparing the 2 techniques' efficiency under similar contrast.

(a)		(b)	
Image size	256×256	Image size	256×256
Voxel size	1.0mm×1.0mm×5.0 mm	Voxel size	1.0mm×1.0mm×5.0 mm
TR	100 ms	TR	6 ms
TE	3 ~ 69 ms (6ms increment)	TE	3 ms
Flip angle	20°	Flip angle	10°
Number of acquisition	12	N (Number of acquisition = N)	7      12
Effective scan time	26 s	Middle F-state	F3      F5
		Gradient spoiler shift	34 lines      20 lines
		Effective scan time (Exclude dummy scan)	11 s      18 s

Table 2: MRI phantom experiment scanning parameters for pulse sequences  
 (a) Multi-echo SPGR (multi-echo FLASH) (b) N-periodic ka-SPGR

#### 4.2.2 Image processing

The F-states images of ka-SPGR were reconstructed from raw data as described in Theory and Figure 2b using MATLAB (Provided by Dr Peter J Lally) and transferred to Python for further processing [12]. The multi-echo SPGR images were also reconstructed from raw data using MATLAB, instead of directly using the default DICOM file from the MRI scanner to ensure consistent post-processing. A mask shown in Figure 6 was extracted from the phantom MR image and used to exclude areas outside the fiducial spheres. The decay time-related images (multi-echo SPGR), or F-states images (ka-SPGR) were masked, and then fitting was performed as shown in Figure 2 to compute T2\* values for each pixel. As the range of interest for T2\* is around 13ms - 53ms for Parkinson's disease, the phantom spheres with T2\* largely outside this range were excluded for further analysis.

The quantitative T2\* mapping images for both techniques were generated by colour-coding the T2\* values obtained on top of a greyscale averaged image of the multiple acquisitions.

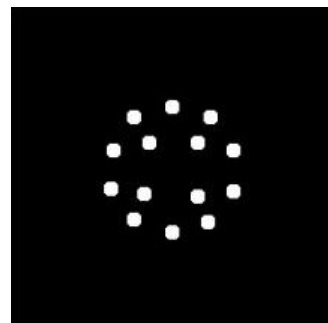


Figure 6: The mask used to extract only fiducial spheres of the Phantom

#### 4.2.3 Analysis method

The T2\* percentage error was computed to evaluate the accuracy of ka-SPGR T2\* measurement in reality, with the ground truth for each voxel defined by the T2\* measured with 90° flip angle multi-echo SPGR. Taking into account the variation caused by the gold-standard technique's measurement variability, a percentage error < 10% would be acceptable in order to detect the change.

The Effective T2\* SNR of ka-SPGR and multi-echo SPGR were calculated to compare their efficiency using the equation,

$$T2^*SNR_{effective} = \frac{mean(T2^*)}{\sigma(T2^*) \times \sqrt{t_{effective}}} \quad (4)$$

All factors that affect the efficiency - the effective time ( $t_{effective}$ ), the number of acquisitions required and the T2\* measurement variation are considered in the above equation. Also, to match the image contrast between acquisitions, 20° flip angle multi-echo SPGR was used for the comparison.

## 5 Results

The computer simulation and MRI phantom scanning experiment results are presented below.

### 5.1 Model simulation results

#### 5.1.1 Optimal N-periodic ka-SPGR parameter

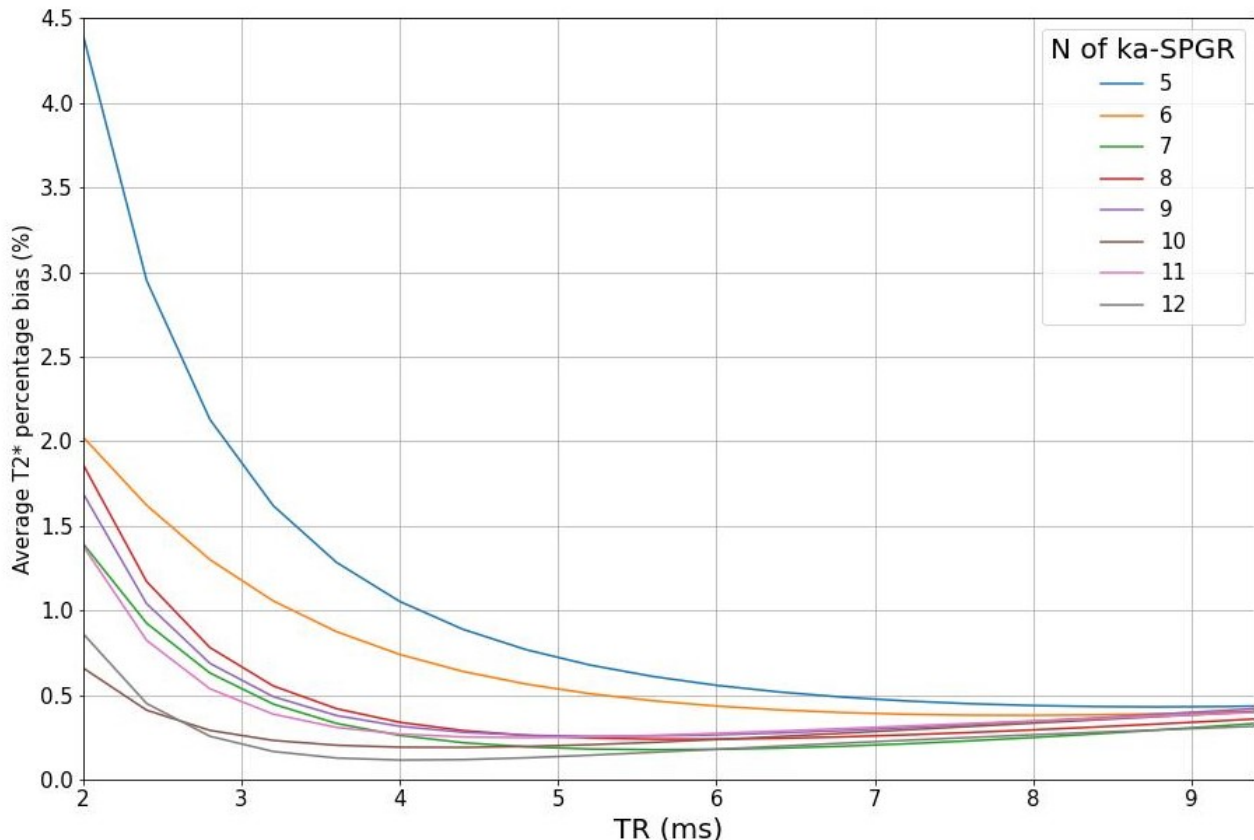


Figure 7: Each line plot shows the changing of the average  $T2^*$  percentage bias with TR for a specific periodic ka-SPGR sequence, and the plots for 5-12 periodic ka-SPGR are shown in the graph using different colours.

The average  $T2^*$  percentage error in the PD biomarker detection range (13-53ms) was calculated for the simulated data of ka-SPGR with Ns and TRs listed in Table 1. By plotting the average percentage error against TR for each periodic ka-SPGR as shown in Figure 7, it was found that the smallest bias of 0.12% can be achieved using 12-periodic ka-SPGR with TR = 4ms. However, constrained by the minimum 6ms TR that the MRI scanner used in this project can achieve, 7-periodic and 12-periodic ka-SPGR with TR = 6ms were used in the scanning experiments, which has a bias of 0.18%.

### 5.1.2 Optimal N-periodic ka-SPGR accuracy and precision

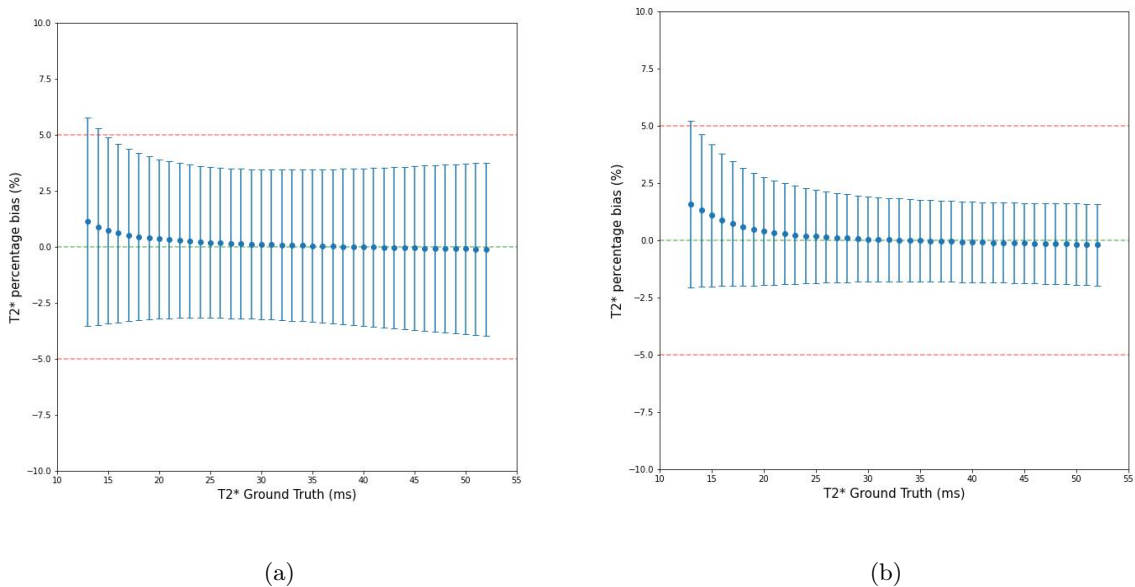


Figure 8: The simulated T2\* percentage bias and the error bar for the 7-periodic (a) and 12-periodic (b) ka-SPGR with TR = 6ms are shown in the plots. A green dotted line shows the zero bias and red dotted lines show  $\pm 5\%$  bias.

The Figure 8 shows the bias and variation of the simulated T2\* values at different ground truth values using 7-periodic ka-SPGR (8a) and 12-periodic ka-SPGR (8b). As shown in the graph, for both ka-SPGR sequences the percentage bias roughly lay on the zero-bias line without obvious variations and the error bars are all approximately inside the  $\pm 5\%$  bias line. The 2 ka-SPGR sequences have about the same percentage bias, however, the 7-periodic ka-SPGR has a two times significantly larger standard deviation than the 12-periodic.

## 5.2 Phantom MRI scan results

### 5.2.1 Quantitative T2\* mapping image

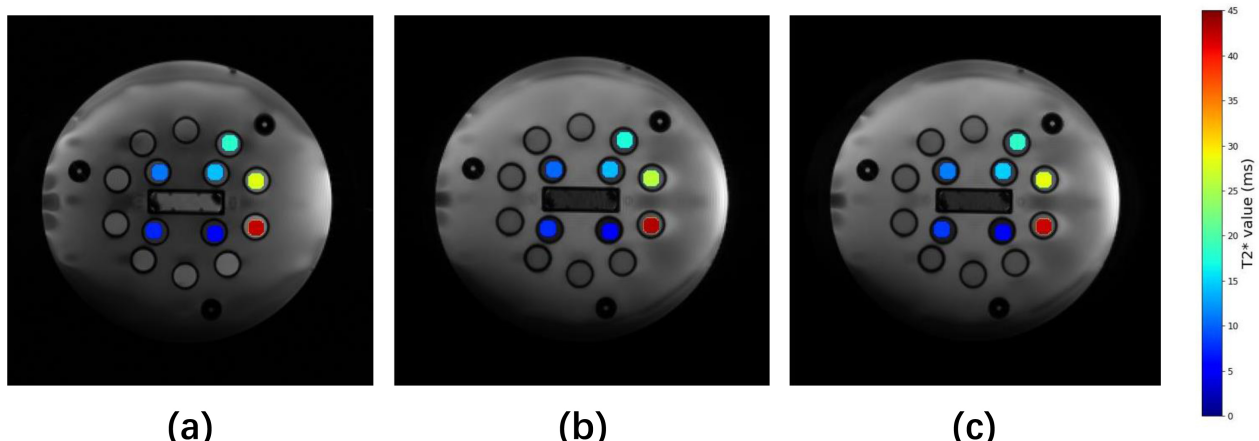
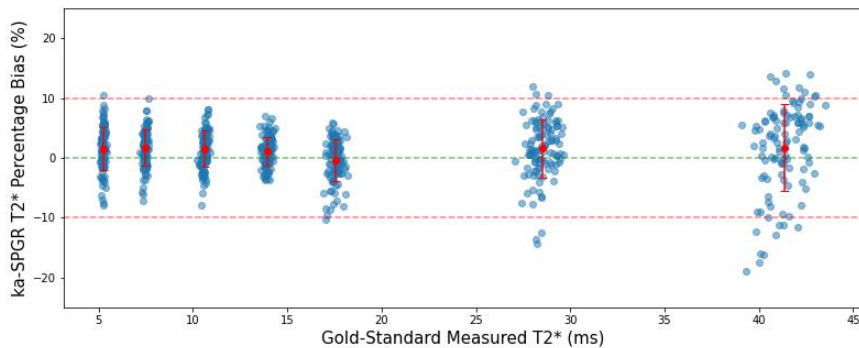


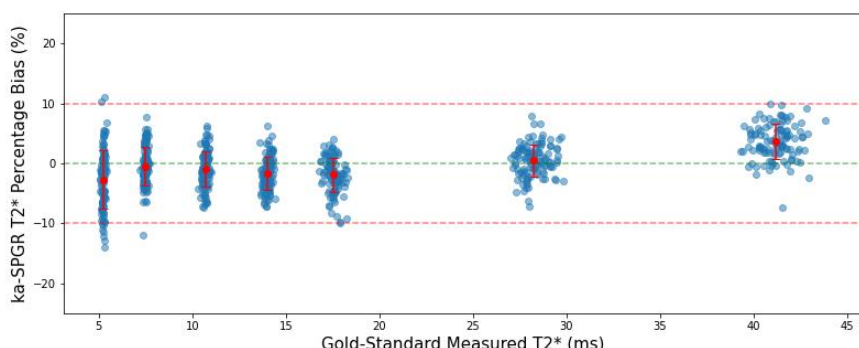
Figure 9: The quantitative T2\* mapping images of the phantom using (a) gold-standard multi-echo SPGR, (b) 7-periodic ka-SPGR and (c) 12-periodic ka-SPGR with the same colourmap. Only the fiducial spheres with PD biomarker-related T2\* are mapped on top of the greyscale image.

As shown in Figure 9, the fitted  $T2^*$  of each fiducial sphere is approximately the same in all 3  $T2^*$  mapping images, which shows the ka-SPGR  $T2^*$  mapping result (Figure 9b c) aligns with the gold standard (Figure 9a). Additionally, there are no large variations of the fitted  $T2^*$  in each fiducial sphere.

### 5.2.2 Percentage bias



(a) 7-periodic ka-SPGR



(b) 12-periodic ka-SPGR

Figure 10: The percentage bias calculated for each voxel is scattered as blue dots, and the mean is plotted in red with an error bar for each fiducial sphere. A horizontal green dotted line is used to show the zero bias, with two red dotted lines showing the  $\pm 10\%$  bias.

The  $T2^*$  percentage bias is computed for each voxel and plotted in Figure 10, each group of points are voxels from the same fiducial sphere and distributed along the x-axis according to the voxel's ground truth  $T2^*$  value (as determined from the multi-echo SPGR). Each group's mean and standard deviation are calculated and plotted as a red error bar on top of the scattered points. For both 7-periodic and 12-periodic ka-SPGR, the mean bias of each fiducial sphere (red dot) stays within  $\pm 5\%$  bias, and all the error bars lay inside  $\pm 10\%$  bias for both plots. Additionally, the 12-periodic ka-SPGR has smaller standard deviations compared with the 7-periodic, especially when measuring a higher  $T2^*$  value.

### 5.2.3 Effective T2\* Signal-to-Noise (SNR) ratio

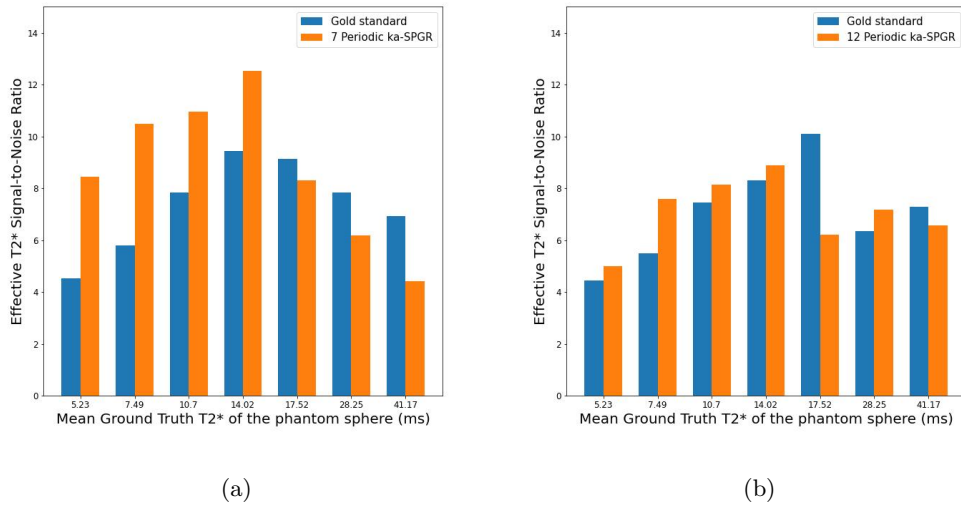


Figure 11: The bar charts show the effective T2\* SNR when using the (a) 7-periodic/ (b) 12-periodic ka-SPGR (orange) and the multi-echo SPGR (blue) for each fiducial sphere and the bars are arranged according to increasing T2\* order, with the mean ground truth T2\* for each sphere labelled on the x-axis.

The effective T2\* SNR of 2 optimal ka-SPGR sequences and multi-echo SPGR are compared in the bar chart (Figure 11), and the bars are arranged in increasing T2\* order in the x-axis. Both 7-periodic and 12-periodic ka-SPGR have a higher effective T2\* SNR than the multi-echo SPGR for measuring a small T2\* value of around 5-15ms, notice that the 7-periodic ka-SPGR exhibits a significantly high-efficiency improvement of about 40% at this range. At higher T2\* values, both ka-SPGR sequences have similar effective T2\* SNR as the multi-echo SPGR, with no improvement observed.

## 6 Discussion and Conclusion

### *Result Discussion*

The optimal 6ms TR 7- and 12-periodic ka-SPGR sequences are both proved to achieve an accurate and precise T<sub>2\*</sub> value measurement with less than  $\pm 5\%$  bias by computer simulation and less than  $\pm 10\%$  bias by MRI phantom scan results (Figure 8, 10). Compared to previous work on T<sub>2\*</sub> mapping at SN using multi-echo SPGR which has a percentage error of around 8-15%, it supports that the optimised ka-SPGR sequence can be used to detect T<sub>2\*</sub> in the PD biomarker detection range. In Figure 10b, an unexpected significant bias is found for the highest T<sub>2\*</sub> value fiducial spheres, which could be related to the increasing bias and variation of the gold-standard multi-echo SPGR technique. This variation of the multi-echo SPGR technique can also be observed in the T<sub>2\*</sub> mapping image constructed in previous studies [21].

The T<sub>2\*</sub> mapping images (Figure 9) obtained and the effective T<sub>2\*</sub> SNR (Figure 11) both support the alignment of the ka-SPGR technique result with the gold-standard technique and suggest that it can be considered as an alternative T<sub>2\*</sub> measuring method to the traditional technique. Additionally, the T<sub>2\*</sub> mapping images also show the ability to distinguish PD (around 10ms) and healthy (around 40ms) SN T<sub>2\*</sub>. As the fitted T<sub>2\*</sub> values in each fiducial sphere are homogenous and do not have voxels containing extremely out-of-range T<sub>2\*</sub> values, this shows the measurement variation will not affect the identification of the PD biomarker, and ka-SPGR T<sub>2\*</sub> mapping image can be potentially used for PD biomarker detection.

Comparing the optimised ka-SPGR sequences, both simulation and phantom scanning results suggest the 12-periodic is a more precise T<sub>2\*</sub> measurement technique and has more tolerance to noise as its standard deviation is almost halved compared to the 7-periodic (Figure 8, 10). It could be explained by the five additional F-states that 12-periodic can reconstruct compared to 7-periodic, as the region data points cover is more favourable [5], the measurement variation decrease. Besides, Figure 11 suggests the T<sub>2\*</sub> measurement efficiency of 7-periodic ka-SPGR is higher than 12-periodic across the PD biomarker detection range and even about 40% higher than the gold-standard T<sub>2\*</sub> measuring technique for small T<sub>2\*</sub> detection when scanning under matched environment. It indicates the 7-periodic ka-SPGR will be a promising technique for detecting T<sub>2\*</sub> PD biomarkers, given its high efficiency in detecting low T<sub>2\*</sub> values. These choices of parameters are also observed in several previous studies, where 12 echoes [3], 7 echoes [12] and similar 8 echoes [5, 1] were used to acquire T<sub>2\*</sub> value.

### *Limitations and Possible Improvements*

However, the study has the following limitations and can be improved. Firstly, the phantom scanning experiment cannot completely represent the ka-SPGR's T<sub>2\*</sub> measurement performance for SN, as the T<sub>1</sub> of the phantom used in this experiment are not specifically aligned with the SN T<sub>1</sub> value. This means the detected signal intensity will be different due to different T<sub>1</sub> and will result in different T<sub>2\*</sub> measurement efficiency for both the ka-SPGR and gold-standard techniques. To perform a more realistic analysis for SN, the phantom sphere should be designed to align with the SN's T<sub>1</sub> and T<sub>2</sub>. Secondly, as the T<sub>2\*</sub> ground truth value for the phantom scanning experiment is measured using the multi-echo SPGR sequence, the obtained ground truth T<sub>2\*</sub> value has variation and bias that will affect the analysis. One possible solution is using a phantom specifically designed for T<sub>2\*</sub> mapping with known ground truth T<sub>2\*</sub> values for each fiducial sphere. Last but not least, as the *in vivo* environment is much more complex than an ideal MRI phantom, the phantom scanning experiment is not enough to fully support ka-SPGR's ability for detecting the PD biomarker *in vivo*. Therefore, *in vivo* MRI scan experiments should be carried out to analyse ka-SPGR performance in more complex environments and a large number of *in vivo* tests would

be required to statistically support that T<sub>2\*</sub> measurement using ka-SPGR can be used for PD biomarker detection. Furthermore, the optimal parameters suggested in this study can be extended to perform in vivo experiments for exploring the motion robustness of the ka-SPGR, which is potentially a huge advantage compared with other existing techniques.

### ***Conclusion***

This study has found that using a 7- or 12-periodic ka-SPGR sequence with TR = 6ms can achieve acceptable accurate and precise measurement of T<sub>2\*</sub> in the PD biomarker detection range. To perform a more efficient scan, 7-periodic ka-SPGR is more favourable and will be able to detect the PD-related T<sub>2\*</sub> drop effectively. With no time limitation, 12-period will be a better choice as it is more robust to noise. However, an MRI phantom designed using SN tissue property with known T<sub>2\*</sub> is highly desirable to perform a more accurate analysis of ka-SPGR T<sub>2\*</sub> mapping performance and further in vivo experiments are essential to support the optimised ka-SPGR's ability to detect PD biomarker.

## 7 Acknowledgements

I gratefully acknowledge Dr Neal Bangerter, for all of the support he provided, especially those valuable workshops he holds for us project students, I learnt treasured research skills and MRI knowledge that would benefit me for a lifetime. He has always given precious advice and feedback, pointing me towards the right direction. I'm thankful to get the opportunity to work in his research group, I will always remember this amazing year I spend in this great group.

I couldn't success this project without the help of Dr Pete Lally. He tirelessly talked me through the concepts of the ka-SPGR technique and patiently answered all of the questions I raised. I acknowledge the scanning session he arranged for helping me perform the MRI phantom experiment and the MATLAB code he provided for processing the raw MRI data. I wouldn't be more fortunate to work with him and learn all this valuable knowledge from him.

I appreciate the support I got from Zimu Huo, he provided the Bloch simulation in C language, which is amazingly fast and saves me loads of time for simulating data. I also thank him for all the inspiring and valuable discussions, his passion for MRI hugely influenced me and it's been my pleasure to work with him.

I would also love to acknowledge the Phd students in the research group: Krithika, Simran, Haeefah, and Michael. I appreciate all the journal club presentations they made, from which I learnt loads of MRI techniques. Studying in a group like this has been a completely joyful experience.

I thank all my fellow students in the research group, they are all amazing people to work with. I thank my friends, Rachel, Wendy, Xiaoxi and Isa, they have encouraged me a lot and given me happiness, I would not successfully finish my final year project without their support.

Lastly, I thank my family, Mom and Dad are always respective and supportive of all the decisions I made. they give me the opportunity to study at Imperial. I gratefully appreciate their encouragement throughout the year and the mental support they provide, I wouldn't survive the college and the final year project without them. I thank my cats, Qiqi, Xiaoshuai, and Huli, for every lovely video and picture, they gave me the power to conquer difficulties.

*Dedicate to my cat, my family member Qiqi who left me forever this year, I believe she's still around me supporting me and will be proud of what I achieved. r.i.p.*

Yifei Jin  
London, United Kindom  
June 15, 2023

## References

- [1] Simon Baudrexel, Lucas Nürnberger, Udo Rüb, Carola Seifried, Johannes C. Klein, Thomas Deller, Helmuth Steinmetz, Ralf Deichmann, and Rüdiger Hilker. Quantitative mapping of t1 and t2 discloses nigral and brainstem pathology in early parkinson's disease. *NeuroImage*, 51:512–520, 2010.
- [2] Daniela Berg, Wolfgang Roggendorf, Ute Schröder, Rüdiger Klein, Thomas Tatschner, Peter Benz, Oliver Tucha, Michael Preier, Klaus W. Lange, Karlheinz Reiners, Manfred Gerlach, and Georg Becker. Echogenicity of the Substantia Nigra: Association With Increased Iron Content and Marker for Susceptibility to Nigrostriatal Injury. *Archives of Neurology*, 59(6):999–1005, 06 2002.
- [3] Malte Brammerloh, Markus Morawski, Isabel Friedrich, Tilo Reinert, Charlotte Lange, Primož Pelicon, Primož Vavpetič, Steffen Jankuhn, Carsten Jäger, Anneke Alkemade, and et al. Measuring the iron content of dopaminergic neurons in substantia nigra with mri relaxometry. *NeuroImage*, 239:118255, Oct 2021.
- [4] Govind B. Chavhan, Paul S. Babyn, Bejoy Thomas, Manohar M. Shroff, and E. Mark Haacke. Principles, techniques, and applications of t2\*-based mr imaging and its special applications. *Radiographics*, 29:1433–1449, 9 2009.
- [5] Hai Ling Margaret Cheng, Nikola Stikov, Nilesh R. Ghugre, and Graham A. Wright. Practical medical applications of quantitative mr relaxometry. *Journal of Magnetic Resonance Imaging*, 36:805–824, 10 2012.
- [6] D. T. Dexter, F. R. Wells, A. J. Lee, F. Agid, Y. Agid, P. Jenner, and C. D. Marsden. Increased nigral iron content and alterations in other metal ions occurring in brain in parkinson's disease. *Journal of Neurochemistry*, 52:1830–1836, 1989.
- [7] Jeff H. Duyn. Steady state effects in fast gradient echo magnetic resonance imaging. *Magnetic Resonance in Medicine*, 37:559–568, 1997.
- [8] Richard R. Ernst, Geoffrey Bodenhausen, and Alexander Wokaun. *Principles of Nuclear Magnetic Resonance in one and two dimensions*. Clarendon Press, 2004.
- [9] Carl Ganter. Steady state of echo-shifted sequences with radiofrequency phase cycling. *Magnetic Resonance in Medicine*, 56:923–926, 2006.
- [10] HáKon Gudbjartsson and Samuel Patz. The rician distribution of noisy mri data. *Magnetic Resonance in Medicine*, 34:910–914, 1995.
- [11] Samantha J. Holdsworth, Mahdi Salmani Rahimi, Wendy W. Ni, Greg Zaharchuk, and Michael E. Moseley. Amplified magnetic resonance imaging (amri). *Magnetic Resonance in Medicine*, 75:2245–2254, 6 2016.
- [12] Peter J Lally, Mark Chiew, Paul M Matthews, Karla L Miller, and Neal K Bangerter. A motion-robust, short-tr alternative to multi-echo spgr.
- [13] Christian Langkammer, Nikolaus Krebs, Walter Goessler, Eva Scheurer, Franz Ebner, Kathrin Yen, Franz Fazekas, and Stefan Ropele. Quantitative mr imaging of brain iron: A postmortem validation study. *Radiology*, 257(2):455–462, Nov 2010.
- [14] Sen Ma, Nan Wang, Yibin Xie, Zhaoyang Fan, Debiao Li, and Anthony G. Christodoulou. Motion-robust quantitative multiparametric brain mri with motion-resolved mr multitasking. *Magnetic Resonance in Medicine*, 87:102–119, 1 2022.
- [15] W. R. Wayne Martin, Marguerite Wieler, and Myrlene Gee. Midbrain iron content in early parkinson disease. *Neurology*, 70(16 Part 2):1411–1417, 2008.

- [16] N. Maserejian, L. Vinikoor-Imler, and A. Dilley. Estimation of the 2020 global population of parkinson's disease (pd)[abstract]. *mov disord.* 2020; 35 (suppl 1).
- [17] Ricarda A. Menke, Jan Scholz, Karla L. Miller, Sean Deoni, Saad Jbabdi, Paul M. Matthews, and Mojtaba Zarei. Mri characteristics of the substantia nigra in parkinson's disease: A combined quantitative t1 and dti study. *NeuroImage*, 47:435–441, 8 2009.
- [18] Dwight G. Nishimura. *Principles of Magnetic Resonance Imaging*. Lulu.com, 2010.
- [19] Werner Poewe, Klaus Seppi, Caroline M. Tanner, Glenda M. Halliday, Patrik Brundin, Jens Volkmann, Anette Eleonore Schrag, and Anthony E. Lang. Parkinson disease. *Nature Reviews Disease Primers*, 3:1–21, 3 2017.
- [20] Stefan Theodor Schwarz, Olivier Mougin, Yue Xing, Anna Blazejewska, Nin Bajaj, Dorothee P. Auer, and Penny Gowland. Parkinson's disease related signal change in the nigrosomes 1–5 and the substantia nigra using t2\* weighted 7t mri. *NeuroImage: Clinical*, 19:683–689, 1 2018.
- [21] Seonyeong Shin, Seong Dae Yun, and N. Jon Shah. T2\* quantification using multi-echo gradient echo sequences: a comparative study of different readout gradients. *Scientific Reports*, 13, 12 2023.
- [22] Matthias Weigel. Extended phase graphs: Dephasing, rf pulses, and echoes - pure and simple. *Journal of Magnetic Resonance Imaging*, 41:266–295, 2 2015.
- [23] Dmitriy A. Yablonskiy and E. Mark Haacke. Theory of nmr signal behavior in magnetically inhomogeneous tissues: The static dephasing regime. *Magnetic Resonance in Medicine*, 32:749–763, 1994.